PHYSICAL REVIEW FLUIDS **3**, 123801 (2018)

Rayleigh-Darcy convection with hydrodynamic dispersion

Baole Wen,[1,2,*] Kyung Won Chang,[2,†] and Marc A. Hesse[1,2,‡]
[1] *Institute of Computational Engineering and Sciences, The University of Texas at Austin,*
Austin, Texas 78712, USA
[2] *Department of Geological Sciences, Jackson School of Geosciences, The University of Texas at Austin,*
Austin, Texas 78712, USA

(Received 27 February 2018; published 7 December 2018)

We investigate the effect of hydrodynamic dispersion on convection in porous media by performing direct numerical simulations (DNS) in a two-dimensional Rayleigh-Darcy domain. Scaling analysis of the governing equations shows that the dynamics of this system are not only controlled by the classical Rayleigh-Darcy number based on molecular diffusion, Ra_m, and the domain aspect ratio, but also controlled by two other dimensionless parameters: the dispersive Rayleigh number $\mathrm{Ra}_d = H/\alpha_t$ and the dispersivity ratio $r = \alpha_l/\alpha_t$, where H is the domain height and α_t and α_l are the transverse and longitudinal dispersivities, respectively. For $\Delta = \mathrm{Ra}_d/\mathrm{Ra}_m > O(1)$, the influence from the mechanical dispersion is minor; for $\Delta \lesssim 0.02$, however, the flow pattern is determined by Ra_d while the convective flux is $F \sim c(\mathrm{Ra}_d)\mathrm{Ra}_m$ for large Ra_m. Our DNS results also show that the increase of mechanical dispersion, i.e., decreasing Ra_d, will coarsen the convective pattern by increasing the plume spacing. Moreover, the inherent anisotropy of mechanical dispersion breaks the columnar structure of the megaplumes at large Ra_m, if $\mathrm{Ra}_d < 5000$. This results in a fan-flow geometry that reduces the convective flux.

DOI: 10.1103/PhysRevFluids.3.123801

I. INTRODUCTION

Convection in porous media controls mass and energy transfer in many natural and engineered applications [1–4]. This subject has received renewed interest because of its potential impact on geological carbon dioxide (CO_2) storage, which allows large reductions of CO_2 emissions from fossil-fuel-based electricity generation [5–7]. After the CO_2 is injected into the deep saline aquifers, it dissolves into the brine and increases the brine density. The dissolution of CO_2 eventually forms a stable stratification and ensures secure long-term storage [8,9].

The rate of CO_2 dissolution is limited by mass transfer of dissolved CO_2 away from the CO_2-brine interface. Diffusive mass transport may take millions of years to saturate the brine [10–12]. However, once the diffusive boundary layer of dissolved CO_2 in brine has grown thick enough, it might become unstable and subsequently convection sets in and forms descending CO_2-rich plumes. This process greatly increases the CO_2 dissolution rate and significantly reduces the leakage risk of buoyant CO_2 into potable aquifers or into the atmosphere [13].

Dynamics of porous media convection can be studied in either a one-sided system where convection is driven by a source of buoyancy on only one boundary, e.g., the solutal convection system [14–20], or a two-sided system where both of top and bottom boundaries actively drive

---

[*] wenbaole@gmail.com
[†] Present address: Geomechanics Department, Sandia National Laboratories, Albuquerque, NM 87123, USA.
[‡] mhesse@jsg.utexas.edu

the convection, e.g., the thermal convection system [17,21–25]. These two systems share many common characteristics in convective pattern and transport properties, although dynamics in the former generally evolve over time while there exists a statistically steady state in the latter [12,17,19,23,26,27]. In this study, we focus on the two-sided convective system (Rayleigh-Darcy convection) to perform long-time direct numerical simulations (DNS) for reliable averaged results.

In the absence of mechanical dispersion, the flow pattern and transport flux of convection in porous media are generally thought to be controlled by the molecular Rayleigh number,

$$\mathrm{Ra}_m = \frac{k\triangle\rho g H}{\mu\phi D_m}, \tag{1}$$

where k is the medium permeability, $\triangle\rho$ is the density change between the fresh and the saturated water, g is the acceleration of gravity, H is the domain height, μ is the dynamic viscosity of the fluid, ϕ is the porosity, and D_m is the molecular diffusion coefficient. At large Ra_m, convection appears in the form of columnar plumes fed continually with a series of protoplumes generated from the diffusive boundary layer [23,25]. As Ra_m is increased, the interplume spacing δ and the flux F in the quasisteady convective regime follow specific power-law scalings of Ra_m, i.e., $\delta \sim \mathrm{Ra}_m^{-\alpha}$ with the positive exponent $\alpha \leqslant 0.5$ [17,23–26,28,29], and $F \approx c\mathrm{Ra}_m$ [19,22,23,25–27,29–34], where $c \approx 0.0068$ for the two-sided system and $c \approx 0.017$ for the one-sided system with fixed CO_2-water contact at the top boundary [19,23,26,29,30,35].

Nevertheless, recent bench-top experiments on solutal convection in porous media show that Ra_m does not control the convective pattern in typical granular media, because mechanical dispersion is the dominant dissipative mechanism [36]. Mechanical dispersion in porous media is due to nonuniformities in the flow that cause mixing of the solute [37–39]. The mathematical description of hydrodynamic dispersion on the Darcy scale is a subject of active investigation [40–42]; however, here we consider the commonly used Fickian dispersion tensor [43–50]. In an isotropic and homogeneous porous medium, this tensor is described by two parameters: the longitudinal and transverse dispersivities α_l and α_t, respectively. Therefore, the hydrodynamic dispersion tensor in the fixed Cartesian reference frame can be expressed as

$$\mathbf{D}^* = D_m\mathbf{I} + (\alpha_l - \alpha_t)\frac{\mathbf{u}^*\mathbf{u}^*}{|\mathbf{u}^*|} + \alpha_t|\mathbf{u}^*|\mathbf{I}, \tag{2}$$

where $\mathbf{I}$ denotes the identity tensor and the mechanical dispersion scales linearly with the interstitial fluid velocity $\mathbf{u}^*$. As long as $|\mathbf{u}^*| \ll D_m/\alpha_l$, $\mathbf{D}^* \approx D_m\mathbf{I}$, so that molecular diffusion dominates over hydrodynamic dispersion; when $|\mathbf{u}^*| \gg D_m/\alpha_l$, however, the mechanical dispersion starts to dominate.

Recent studies [36,46–54] indicate that hydrodynamic dispersion significantly affects the flow pattern and mass transport of convection in porous media under certain conditions. Numerical simulations [47,48] show that hydrodynamic dispersion enhances the convective mixing and greatly reduces the onset time for convection; however, recent laboratory experiments reveal that the mechanical dispersion coarsens the convective pattern and reduces the increase of convective flux with increasing permeability k [36,51]. Particularly, systematic experiments [36] illustrate that adjusting Ra_m via changing the density difference $\triangle\rho$ or the medium permeability k may result in distinct convective characteristics due to hydrodynamic dispersion. For fixed $\triangle\rho$, increasing k (via choosing a larger glass bead diameter d as $k \sim d^2$) raises Ra_m but *enlarges* the interplume spacing δ; for fixed k, however, δ is nearly fixed for increasing $\triangle\rho$. Second, for fixed $\triangle\rho$, the dissolution flux F does not increase linearly with k and is lower than expected at high k; for fixed k, in contrast, $F \sim c(k)\mathrm{Ra}_m$ with decreasing prefactor c as k is increased. Despite this decrease in flux, the vertical velocity, as measured by the speed of the fastest descending fingertip, increases approximately linearly with both $\triangle\rho$ and k. Some of the above findings contradict the classical predictions made in the absence of mechanical dispersion.

To understand the effect of dispersion on convection, we perform DNS in a two-dimensional (2D), rectangular, homogeneous, and isotropic Rayleigh-Darcy domain. We aim to identify the dimensionless parameters governing convection in porous media with hydrodynamic dispersion, determine the scaling law for the quasisteady convective flux, and quantify the contribution of molecular diffusion and mechanical dispersion to the hydrodynamic dissipation. As mentioned earlier, we focus on a two-sided convective system for long-time averaged results of individual simulations, but the results can be qualitatively applied to the one-sided case due to many common features in convection shared by these two systems [12,17,23,26,27].

The remainder of this paper is organized as follows. In the next section, we nondimensionalize the system in a specific way so that the parameters controlling the pattern and the flux, respectively, are decoupled, and describe the numerical method to solve the dimensionless equations. In Sec. III, we present the DNS results in terms of different control parameters, including both the diffusion-dominant and dispersion-dominant limits. In Sec. IV, we analyze how hydrodynamic dispersion affects the convective pattern and flux, apply our results to recent laboratory experiments of solutal convection in bead packs, compare our results with previous numerical investigations in Refs. [47,48], and discuss the limitations of the Fickian dispersion model. Our conclusions are given in Sec. V.

II. PROBLEM FORMATION AND COMPUTATIONAL METHODOLOGY

In previous studies, the dispersivity, α_l or α_t, and the molecular diffusivity D_m are combined to define the characteristic length and timescales or the Rayleigh number [47,48]. In this work, however, we rescale the system using the domain height H, the buoyancy velocity $U = k\triangle\rho g/(\mu\phi)$, and the convective timescale $T_c = H/U$. As will be discussed in Sec. IV C, different scales for nondimensionalization may lead to opposite conclusions. However, it will be shown below that the scales chosen in this study allow us to decouple the parameters controlling the flow pattern and the flux which simplifies the discussion. Based on these scales, we obtain the dimensionless equations

$$\frac{\partial C}{\partial t} + \mathbf{u}\cdot\nabla C = \nabla\cdot(\mathbf{D}\nabla C), \tag{3a}$$

$$\mathbf{u} = -\nabla p - C\mathbf{e}_z, \tag{3b}$$

$$\nabla\cdot\mathbf{u} = 0, \tag{3c}$$

where C, $\mathbf{u} = (u, w)$, and p are the dimensionless forms of concentration, velocity, and pressure, respectively, and $\mathbf{e}_z$ is a unit vector in z (upward) direction. The dimensionless hydrodynamic dispersion tensor is then given by

$$\mathbf{D} = \mathrm{Ra}_m^{-1}\mathbf{I} + \mathrm{Ra}_d^{-1}\left[(r-1)\frac{\mathbf{uu}}{|\mathbf{u}|} + |\mathbf{u}|\mathbf{I}\right] \tag{4}$$

and characterized by the molecular Rayleigh number $\mathrm{Ra}_m = UH/D_m$ defined in Eq. (1) and two additional parameters,

$$\mathrm{Ra}_d = \frac{UH}{D_t} = \frac{UH}{\alpha_t U} = \frac{H}{\alpha_t} \tag{5a}$$

and

$$r = \frac{\alpha_l}{\alpha_t}, \tag{5b}$$

which are referred to as dispersive Rayleigh number and dispersivity ratio, respectively. Here, $D_t = \alpha_t U$ is the transverse dispersion coefficient, and the definition of the dispersive Rayleigh number is analogous to the definition of Ra_m or the Peclét number based on the longitudinal or transverse dispersion coefficient [55]. Moreover, from the definition, the dissipation by mechanical dispersion increases with decreasing Ra_d. This allows us to easily recover the case without mechanical dispersion and to study the limit of high-Ra_m convection.

It is worth noting that the dimensionless hydrodynamic dispersion tensor can also be written as

$$\mathbf{D} = \frac{1}{\mathrm{Ra}_h}\left\{\frac{\mathbf{I}}{1+1/\Delta} + \frac{1}{1+\Delta}\left[(r-1)\frac{\mathbf{uu}}{|\mathbf{u}|} + |\mathbf{u}|\mathbf{I}\right]\right\} \tag{6}$$

or

$$\mathbf{D} = \frac{1}{\mathrm{Ra}_m}\left\{\mathbf{I} + \frac{1}{\Delta}\left[(r-1)\frac{\mathbf{uu}}{|\mathbf{u}|} + |\mathbf{u}|\mathbf{I}\right]\right\}, \tag{7}$$

where

$$\mathrm{Ra}_h = \frac{UH}{D_m + D_t} = \frac{1}{\frac{1}{\mathrm{Ra}_m} + \frac{1}{\mathrm{Ra}_d}} \tag{8a}$$

and

$$\Delta = \frac{D_m}{D_t} = \frac{\mathrm{Ra}_d}{\mathrm{Ra}_m} \tag{8b}$$

represent the effective Rayleigh number based on hydrodynamic dispersion and the ratio of molecular diffusion to mechanical dispersion, respectively. In addition, $1/\Delta = U\alpha_t/D_m$ can also be interpreted as a microlevel Peclét number based on a pore-scale length, i.e., the dispersivity $\alpha_t \sim d/r$. Therefore, diffusion is the dominant dissipative mechanism for $\Delta \gg 1$, so that $\mathrm{Ra}_h \approx \mathrm{Ra}_m$; similarly, mechanical dispersion is the dominant dissipative mechanism for $\Delta \ll 1$ and $\mathrm{Ra}_h \approx \mathrm{Ra}_d$.

The flow is assumed to be periodic laterally with a impermeable top and bottom boundaries. Solute concentration along the top and bottom boundaries is unity and null, respectively. Hence, the boundary conditions at the top and the bottom are given by

$$C|_{z=1} = 1 \quad \text{and} \quad w|_{z=1} = 0; \quad C|_{z=0} = w|_{z=0} = 0. \tag{9}$$

Note that the problem posed by (3) and (9) is formally identical to the two-sided thermal convection problem in which the domain is heated from below and cooled from above. Here, (3) and (9) are solved numerically using a Fourier-Chebyshev-tau pseudospectral solver developed in Refs. [25,29], the temporal discretization is achieved using a three-step semi-implicit Runge-Kutta scheme [56], and the numerical scheme is parallelized using the message passing interface (MPI). In order to obtain reliable averaged results, the DNS are performed up to $O(10^3)$ convective time units. The dispersivity ratio r can vary from 1 to 30 in various field sites [57], and laboratory experiments and numerical simulations reveal that the transverse dispersivity is usually an order of magnitude less than the longitudinal dispersivity in advection dominated systems [58–62]. Thus, we set $r = 10$ in most simulations, but also explore how r affects both the convective pattern and the flux when mechanical dispersion dominates the hydrodynamic dispersion at $\mathrm{Ra}_d = 1000$.

To quantify the flow, we measure the convective flux F at the top wall,

$$F = \left.\left\langle \overline{\frac{\partial C}{\partial z}} + \frac{\mathrm{Ra}_m}{\mathrm{Ra}_d}\overline{|u|\frac{\partial C}{\partial z}}\right\rangle\right|_{z=1} = F_m + F_d, \tag{10}$$

where the angle bracket and the overbar denote the long-time and the horizontal averages, respectively, the first term on the right side of (10) represents the flux at the boundary via pure molecular diffusion F_m, and the second term represents the flux via mechanical dispersion F_d. We also measure the interplume spacing δ by time averaging the dominant Fourier mode number in the interior, the mean horizontal velocity at the top wall, $\tilde{u} = \langle\overline{|u|}\rangle|_{z=1}$, the mean vertical velocity in the interior, $\tilde{w} = \langle\overline{|w|}\rangle|_{z=\frac{1}{2}}$, and the magnitude of the time-averaged w extremum value in the interior, $w_m = \langle \max(|w|_{z=\frac{1}{2}})\rangle$. In our study, these averaged results are all from individual simulations.

III. RESULTS

To explore the effect of hydrodynamic dispersion on convection, numerical simulations and laboratory experiments can be conducted in different combinations of parameters, e.g., Ra_h and Δ, or density difference $\triangle\rho$ and grain size d. In this study, we perform DNS in terms of fixed (Ra_m, r), (Ra_d, r), and (Ra_m, Ra_d), respectively. It will be shown below for fixed r, the parameters Ra_m and Ra_d predominantly control the flux and the pattern, respectively, in the dispersion-dominated regime. However, in experiments it is difficult to change Ra_d with fixed Ra_m by varying $\triangle\rho$ and d, since the variation of grain size changes both Ra_m and Ra_d simultaneously.

A. Fixed Ra_m and r

Figures 1 and 2 show the variation of the convective flow pattern and the corresponding averaged DNS results as a function of Ra_d for $\mathrm{Ra}_m = 20\,000$ and $r = 10$. When the smallest diffusive length scale $1/\mathrm{Ra}_m$ is much larger than the pore scale of the medium d/H, i.e., $\mathrm{Ra}_d \gg r\mathrm{Ra}_m$ as $\alpha_t \approx d/r$ [38,63], the molecular diffusion dominates the hydrodynamics dispersion [19,23,36]. Our DNS results reveal that only for $\Delta \equiv \mathrm{Ra}_d/\mathrm{Ra}_m \gtrsim 10^5$, the convection with mechanical dispersion converges to the classical columnar flow [Figs. 1(f) and 2].

When $O(1) < \Delta < 10^5$, the relatively weak mechanical dispersion slightly increases the plume width and enhances the convective transport, but the flow still retains the columnar structure [Figs. 1(e), 2(a), and 2(b)]. For $\Delta < O(1)$, however, the mechanical dispersion starts to apparently affect the convective pattern and flux: the convection transitions to a fan flow with laterally expanding megaplumes along the vertical flow direction [Figs. 1(b)–1(d)], and the convective flux is reduced to approximately 50% of the high-Ra_d value at $\Delta = 0.05$ [Fig. 2(a)].

Increasing dispersion thickens the diffusive boundary layer [Fig. 1(a)], smoothes the small-scale plumes near the walls, and stabilizes the flow [Figs. 1(b)–1(f)]. Eventually, the convection becomes steady at $\mathrm{Ra}_d = 100$ [Fig. 1(b)] and the flux is again increased for $\Delta \leqslant 0.05$ due to the large magnitude of the effective diffusion coefficient, $(\mathrm{Ra}_m/\mathrm{Ra}_d)|u|$, induced by the mechanical dispersion [Fig. 2(a)]. Moreover, it is also seen from Figs. 2(b) and 2(c) that hydrodynamic dispersion coarsens the flow pattern, given by δ, and the mean buoyancy velocities at the top and in the interior, $\tilde{u}$, $\tilde{w}$, and w_m, roughly follow the same trend as the convective flux. It should be noted that the w extremum value, w_m, becomes nearly constant for $0.025 \leqslant \Delta \leqslant 0.25$ [Fig. 2(c)].

B. Fixed Ra_d and r

Figures 3 and 4 show the convective pattern and the corresponding averaged DNS results as a function of Ra_m for $\mathrm{Ra}_d = 1000$ and $r = 10$. The convection basically remains a fan-flow structure at $\mathrm{Ra}_d = 1000$ as $\mathrm{Ra}_m \to \infty$ [Figs. 3(b)–3(f)]. In particular, the interplume spacing δ is nearly invariant when $\Delta \lesssim 0.2$ [Fig. 4(b)]; the mean velocities $\tilde{u}$ and $\tilde{w}$ are roughly unchanged after $\Delta \lesssim 0.05$ [Fig. 4(c)]; and the time-averaged horizontal-mean concentration profile $\langle\overline{C}\rangle$ becomes almost fixed for $\Delta \lesssim 0.02$ [Fig. 3(a)], so that at the top and the bottom, the flux due to molecular diffusion (i.e., F_m) levels off [Fig. 4(a)]. In short, at sufficiently large Ra_m, the flow pattern and the averaged system quantities (i.e., $\langle\overline{C}\rangle$, δ, $\tilde{u}$, $\tilde{w}$, and w_m) are *independent* of Ra_m.

Actually, as $\mathrm{Ra}_m \to \infty$, the hydrodynamic dispersion tensor (4) reduces to

$$\mathbf{D} \to \mathrm{Ra}_d^{-1}\left[(r-1)\frac{\mathbf{uu}}{|\mathbf{u}|} + |\mathbf{u}|\mathbf{I}\right], \tag{11}$$

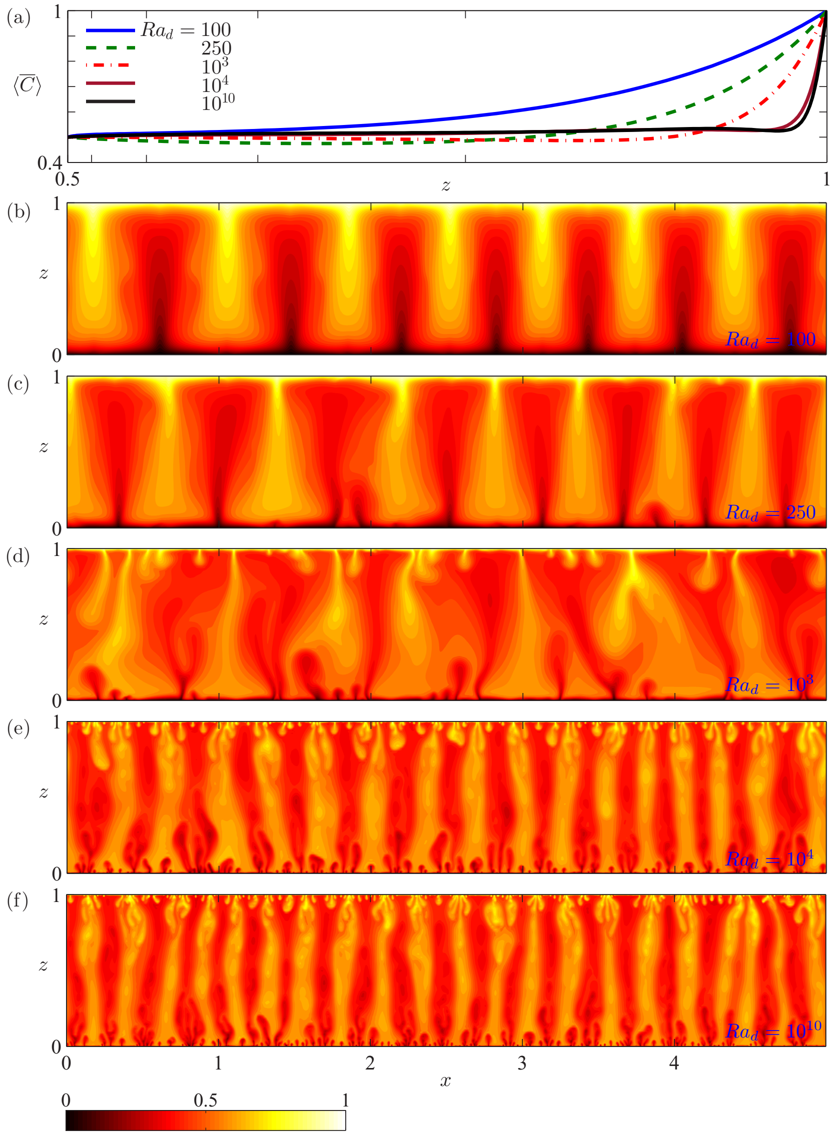

FIG. 1. Time-averaged horizontal-mean concentration profile $\langle\overline{C}\rangle$ and snapshots of the concentration field C from DNS at $\mathrm{Ra}_m = 20\,000$ and $r = 10$ for different Ra_d. The domain aspect ratio is $L = 5$. In panel (a), only half of $\langle\overline{C}\rangle$ is shown due to its antisymmetry about the midplane, and the z values on the horizontal axis are nonuniformly spaced to clearly show the structure near the wall. Increasing mechanical diperison (decreasing Ra_d) thickens the diffusive boundary layer, coarsens the flow pattern, and stabilizes the flow. Moreover, the convection transitions to a fan-flow structure at $\mathrm{Ra}_d < 5000$.

so that Ra_d becomes the only parameter controlling the dynamics of the system for fixed r. Thus, at large Ra_m the concentration field C and the buoyancy velocity $\mathbf{u}$ are determined *solely* by the dispersive Rayleigh number Ra_d, as confirmed by our DNS data. Once C and $\mathbf{u}$ become invariant in the limit of $\mathrm{Ra}_m \to \infty$, $F_m \sim c_1$, and $F_d \sim c_2\mathrm{Ra}_m$ with the constants c_1 and c_2 determined by Ra_d, as shown in Fig. 4(a).

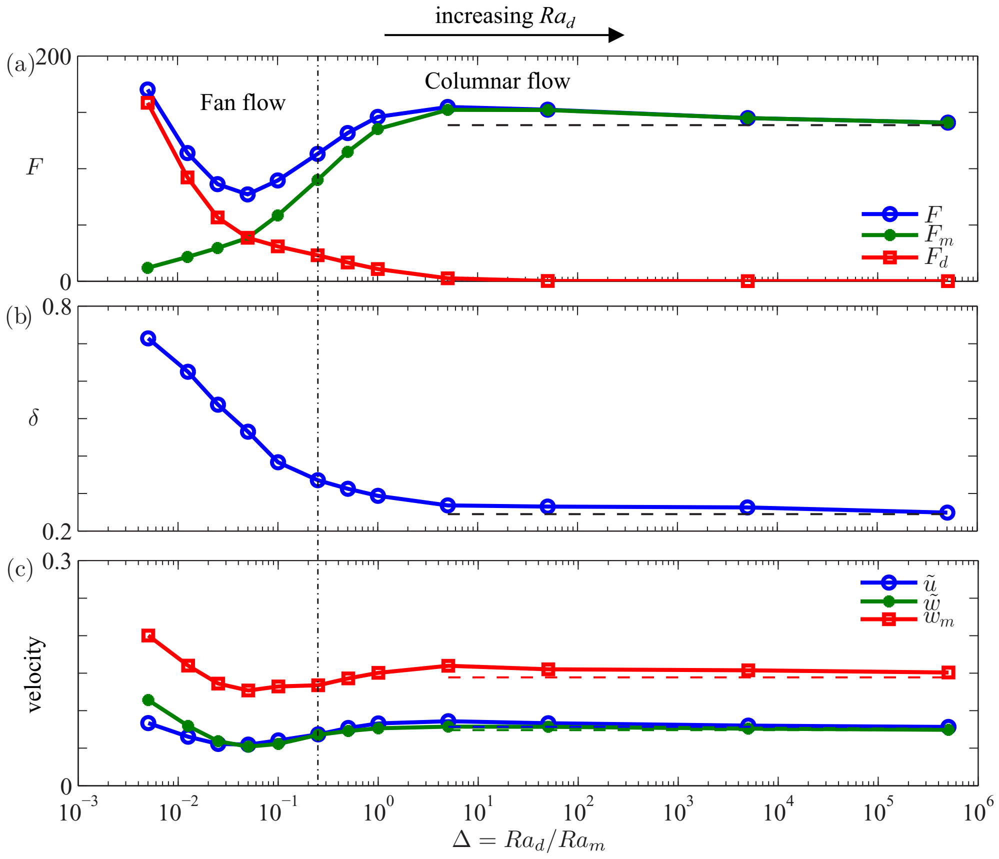

FIG. 2. Averaged DNS results of convection at $\mathrm{Ra}_m = 20\,000$ and $r = 10$ for different Ra_d. The domain aspect ratio is $L = 5$. The dashed lines denote the results in the absence of mechanical dispersion and the dash-dotted line separates the fan-flow and the columnar-flow regions. Relatively weak mechanical dispersion slightly enhances the convective transport. However, as convection transitions to a fan-flow structure, the transport flux is significantly reduced. Nevertheless, in the strong-dispersion limit, the flow is stabilized and the flux is increased again due to the large magnitude of the effective diffusion coefficient.

C. Fixed Ra_m and Ra_d

In this section, we explore how the dispersivity ratio affects the convective pattern and flux at $\mathrm{Ra}_m = 20\,000$ and $\mathrm{Ra}_d = 1000$, corresponding to $\Delta \sim 0.05$ where the reduction of the flux by dispersion is strongest [Fig. 2(a)]. In the fixed domain, constant Ra_d implies invariant transverse dispersivity, so increasing the dispersivity ratio r only strengthens the longitudinal dispersivity.

As in Fig. 3(a), where Ra_d is also fixed, when mechanical dispersion is the dominant dissipative mechanism varying Ra_m or r only slightly changes the boundary-layer thickness [Fig. 5(a)], which is predominantly controlled by the strength of transverse dispersivity (see detailed analysis in Sec. IV A). At $r = 1$, the hydrodynamic dispersion tensor $\mathbf{D}$ is heterogeneous but isotropic, the high-Ra_m convection remains a columnar structure [Fig. 5(b)], and the convective flux is increased compared with that in the absence of mechanical dispersion [Fig. 6(a)]. After adding isotropic velocity-dependent mechanical dispersion, the diffusion boundary layer is thickened so that more saturated water is advected downward and upward by columnar flows from the upper and lower layers. For $r > 1$, however, $\mathbf{D}$ is both heterogeneous and anisotropic, and the convection transitions to a fan-flow structure [Figs. 5(c)–5(e)]. Increasing r monotonically enlarges the interplume spacing

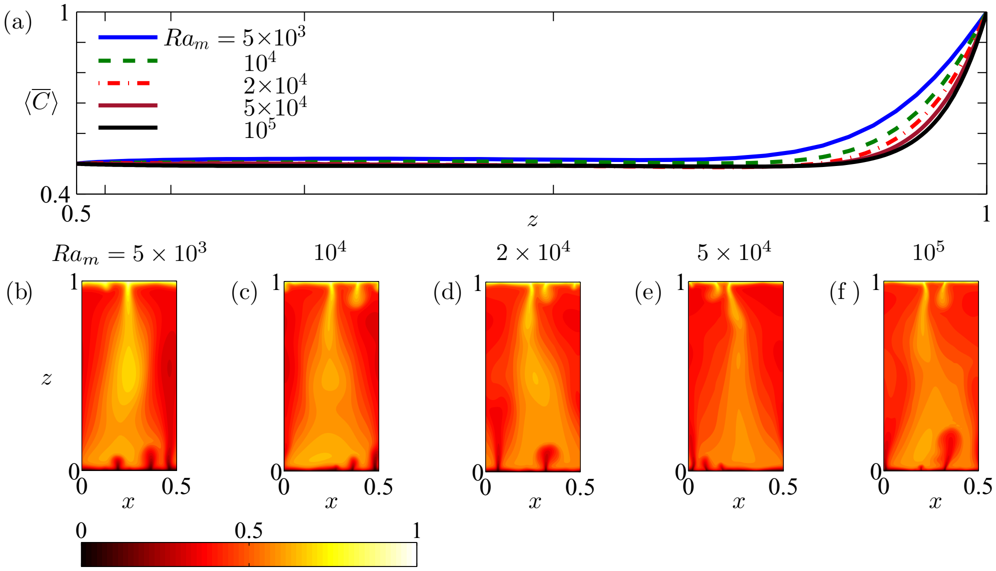

FIG. 3. Time-averaged horizontal-mean concentration profile $\langle\overline{C}\rangle$ and snapshots of the concentration field C from DNS at $\mathrm{Ra}_d = 1000$ and $r = 10$ for different Ra_m. For $\mathrm{Ra}_m \leqslant 20\,000$, the domain aspect ratio is $L = 5$, while for $\mathrm{Ra}_m > 20\,000$, DNS are performed in a small unit $L = 0.5$ where there only exists a single rising and descending megaplume but the turbulent convection still sustains itself. In panel (a), only half of $\langle\overline{C}\rangle$ is shown due to its antisymmetry about the midplane, and the z values on the horizontal axis are nonuniformly spaced to clearly show the structure near the wall. For fixed $\mathrm{Ra}_d = 1000$ and $r = 10$, the averaged and instantaneous concentration fields become nearly invariant at $\mathrm{Ra}_m \gtrsim 50\,000$ (i.e., $\Delta \lesssim 0.02$).

δ [Fig. 6(b)] and decreases the convective flux and buoyancy velocity [Figs. 6(a) and 6(c)]. Finally, for $r \geqslant 10$ the dynamics of the system become nearly invariant. Similar results have been observed in the one-sided convection problem [36].

D. Pattern formation and transport flux in the $(\mathrm{Ra}_m, \mathrm{Ra}_d)$ parameter space

In advection-dominated systems, the dispersivity ratio, $r \sim O(10)$, is generally fixed [58–62]. A natural question concerns how the mechanical dispersion affects convection in the $(\mathrm{Ra}_m, \mathrm{Ra}_d)$ parameter space at $r = 10$. For $\Delta > O(1)$, the influence from the mechanical dispersion is minor, so that both the convective pattern and flux are mostly controlled by Ra_m. For $0.02 \lesssim \Delta < O(1)$, both the molecular diffusion and the mechanical dispersion are important to convection, e.g., they equally affect the flux at $\Delta \approx 0.05$. For $\Delta < 0.02$, the mechanical dispersion dominates the hydrodynamic dispersion: The flow pattern is determined by Ra_d, e.g., $C = C(\mathrm{Ra}_d)$, $\delta = \delta(\mathrm{Ra}_d)$, and $\mathbf{u} = \mathbf{u}(\mathrm{Ra}_d)$, while the flux is predominantly controlled by Ra_m, i.e., $F = F_m + F_d \sim c_1(\mathrm{Ra}_d) + c_2(\mathrm{Ra}_d)\mathrm{Ra}_m \sim c_2(\mathrm{Ra}_d)\mathrm{Ra}_m$. Since Δ represents the ratio of molecular diffusion coefficient to transverse dispersion coefficient, in this study it is used to characterize when the mechanical dispersion becomes the dominant dissipative mechanism at given Ra_m or Ra_d. However, the parameter Δ couples both the media and fluid properties and determines neither the flow pattern nor the convective flux in the macro level. Our DNS results and analysis indicate that in a dispersion-dominated regime (i.e., $\Delta < 0.02$), Ra_d and Ra_m are more effective parameters controlling the pattern and the flux, respectively, throughout the domain.

Determination of the functions $c_1(\mathrm{Ra}_d)$ and $c_2(\mathrm{Ra}_d)$ requires extensive numerical simulations at $\mathrm{Ra}_m > 100\mathrm{Ra}_d$, where mechanical dispersion dominates the dissipation ($\Delta \ll 1$). Here we only show the variations of c_1 and c_2 as a function of Ra_d for $\mathrm{Ra}_d \leqslant 1000$ due to the expensive

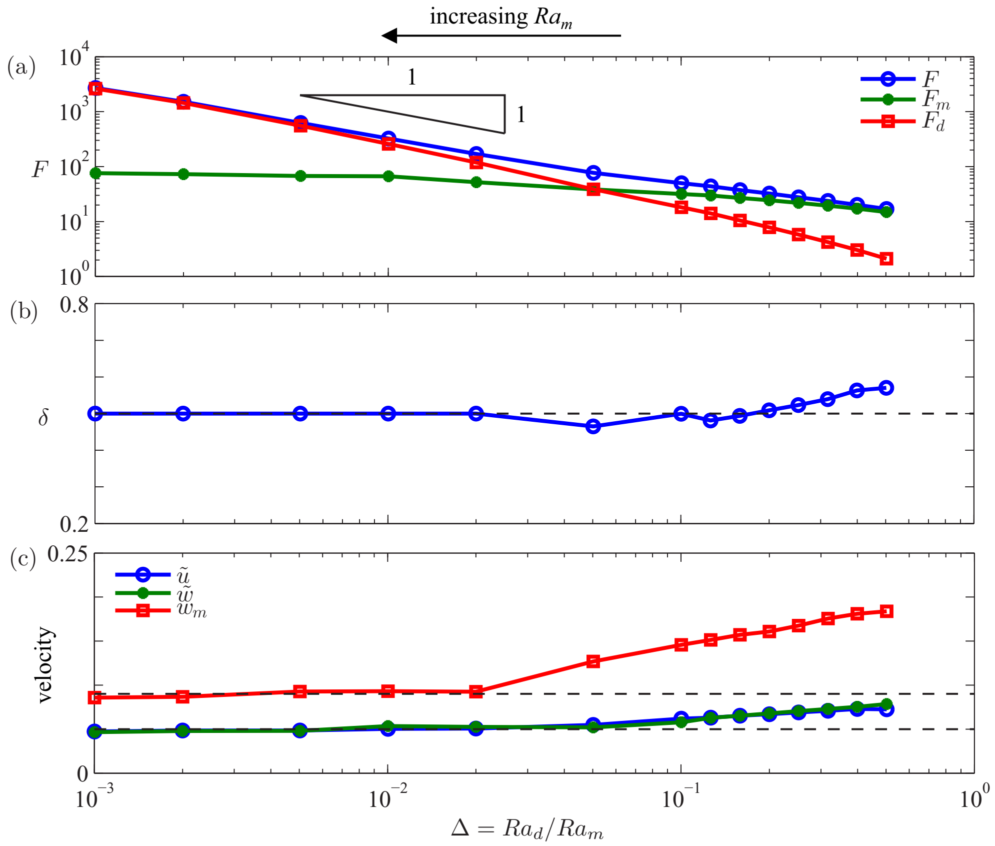

FIG. 4. Averaged DNS results of convection at $\mathrm{Ra}_d = 1000$ and $r = 10$ for different Ra_m. L is as in Fig. 3. For fixed Ra_d and r, the concentration field C, the interplume spacing δ and the buoyancy flow velocity $\mathbf{u}$ become invariant at sufficiently large Ra_m. Hence, as $\mathrm{Ra}_m \to \infty$, the flux by molecular diffusion, $F_m = \langle \partial_z \overline{C} \rangle|_{z=1}$, becomes constant, while the flux by mechanical dispersion, $F_d = \langle \mathrm{Ra}_m/\mathrm{Ra}_d\ \overline{|u|\partial_z C} \rangle|_{z=1}$, increases linearly with Ra_m.

computations (Fig. 7). Our study above shows that the pattern of convection is determined by Ra_d for $\Delta \ll 1$. Increasing dispersion (i.e., decreasing Ra_d) thickens the diffusive boundary layer and decreases the concentration gradient at the wall, thereby monotonically decreasing c_1, i.e., $c_1 \sim \mathrm{Ra}_d^{0.74}$, as shown in Fig. 7(a). Moreover, for $\mathrm{Ra}_d \leqslant 1000$ the prefactor c_2 increases with decreasing Ra_d due to the large magnitude of the effective diffusion coefficient $(\mathrm{Ra}_m/\mathrm{Ra}_d)|u|$, i.e., $c_2 \sim \mathrm{Ra}_d^{-0.51}$, as shown in Fig. 7(b). We note that these scalings may not hold at large Ra_d, where the determination of $c_1(\mathrm{Ra}_d)$ and $c_2(\mathrm{Ra}_d)$ requires more systematic numerical simulations at extremely high Ra_m (to ensure $\Delta \ll 1$).

IV. DISCUSSION

A. Effects of dispersion on convective pattern and flux: Mechanisms

Our DNS results and analysis above reveal that at sufficiently large Ra_m, the convective pattern is determined by the dispersive Rayleigh number Ra_d: The convection appears in the form of columnar flow at $\mathrm{Ra}_d \geqslant 5000$ and then transitions to a fan flow at $\mathrm{Ra}_d < 5000$. This fan-flow structure here is due to the inherent anisotropy of mechanical dispersion. As shown in Fig. 8, near the top and the bottom walls the flow between the neighboring plumes is dominantly horizontal, so

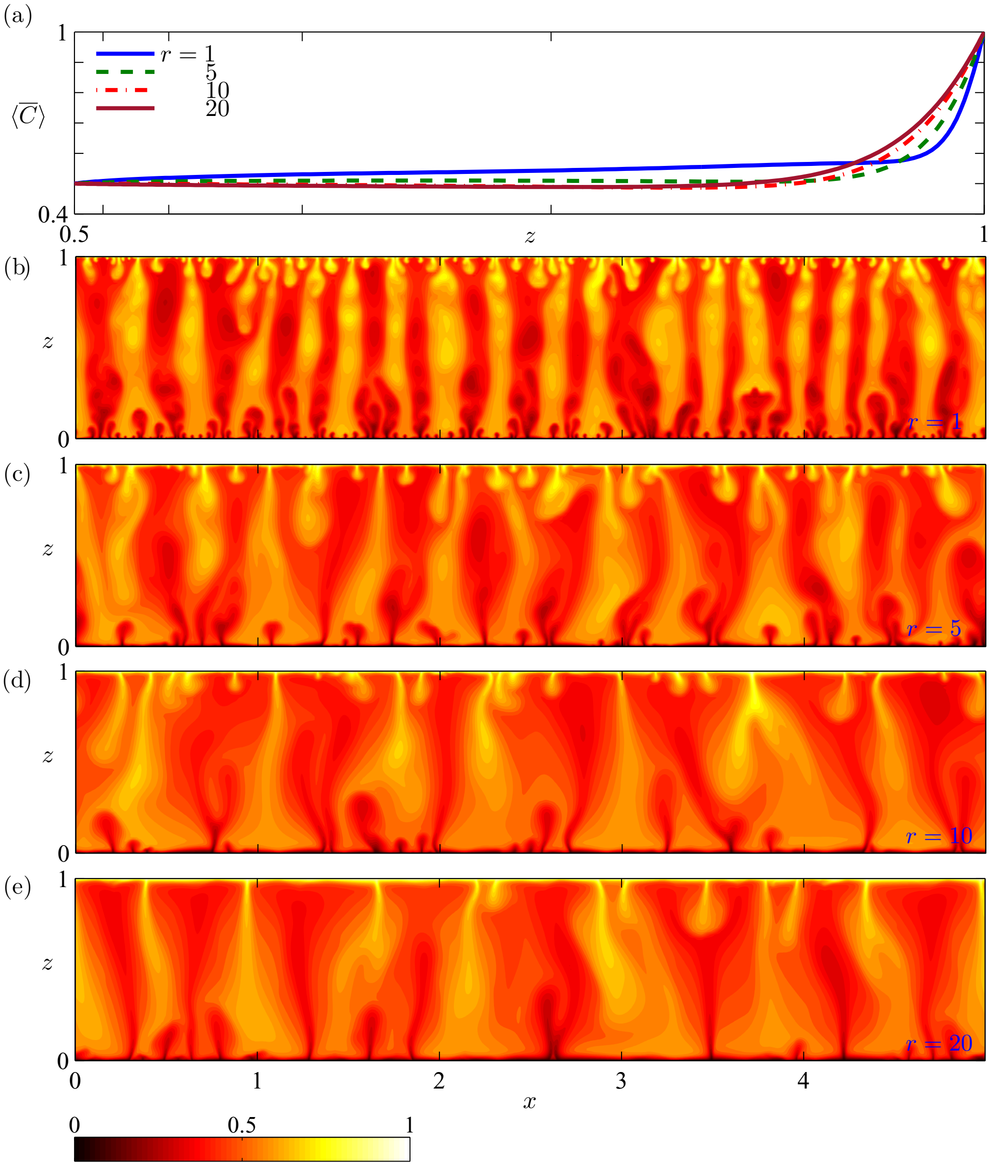

FIG. 5. Time-averaged horizontal-mean concentration profile $\langle\overline{C}\rangle$ and snapshots of the concentration field C from DNS at $\mathrm{Ra}_m = 20\,000$ and $\mathrm{Ra}_d = 1000$ for different r. The domain aspect ratio is $L = 5$. In panel (a), only half of $\langle\overline{C}\rangle$ is shown due to its antisymmetry about the midplane, and the z values on the horizontal axis are nonuniformly spaced to clearly show the structure near the wall. When mechanical dispersion is the dominant dissipative mechanism at $\mathrm{Ra}_d = 1000$, i.e., $\Delta \ll 1$, the high-Ra_m convection in porous media remains a columnar structure at $r = 1$, but transitions to a fan-flow structure at $r > 1$.

the interplume spacing is set by the lateral dispersion due to horizontal flow, $D^*_{xx,w} \approx D_m + \alpha_l u^*_w$, and the thickness of the diffusive boundary layer is significantly affected by the vertical dispersion due to horizontal flow, $D^*_{xz,w} \approx D_m + \alpha_t u^*_w$, where u^*_w is the horizontal velocity at the top and/or bottom wall and all the variables with superscript $*$ are in dimensional form. At the roots of the plumes, however, the flow is dominantly vertical, so the plume width is controlled by the lateral dispersion due to vertical flow, $D^*_{zx,r} \approx D_m + \alpha_t w^*_r$, where w^*_r is the vertical velocity at

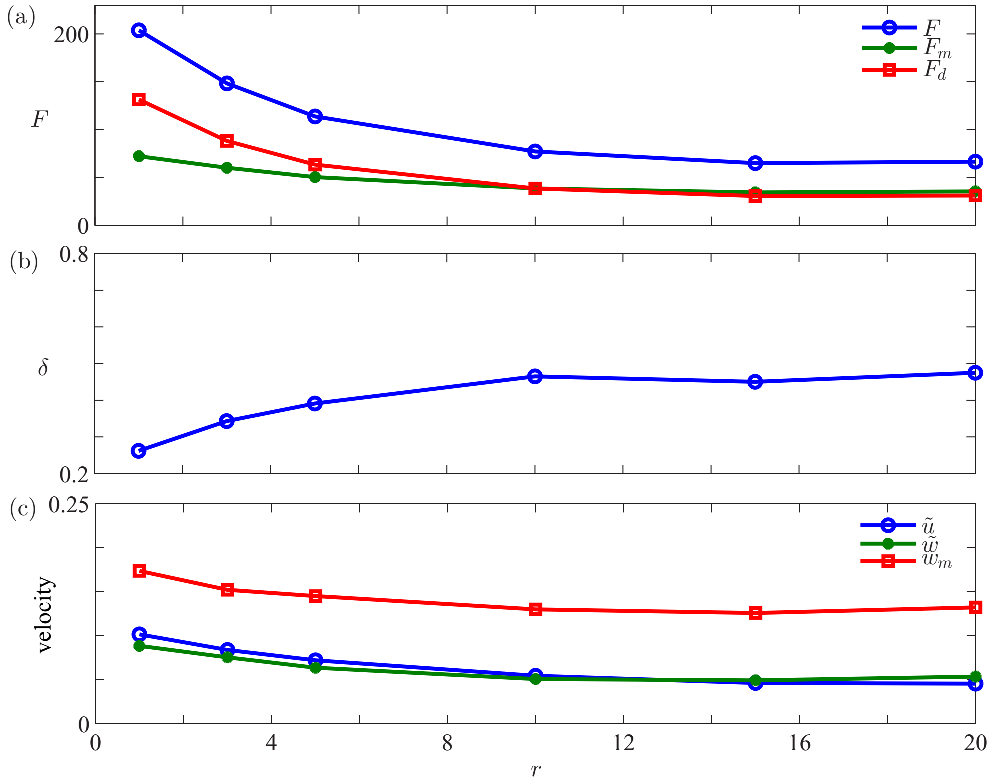

FIG. 6. Averaged DNS results of convection at $\mathrm{Ra}_m = 20\,000$ and $\mathrm{Ra}_d = 1000$ for different r. The domain aspect ratio is $L = 5$. In the absence of mechanical dispersion, the flux $F \approx 138$ at $\mathrm{Ra}_m = 20\,000$, so the mass transport is enhanced after adding isotropic, velocity-dependent dispersion ($r = 1$). Increasing r enlarges the interplume spacing and decreases the convective flux and buoyancy velocity. For $r \geqslant 10$, the averaged results become nearly invariant.

the plume roots. The mass conservation of the incompressible flow requires $u_w^* \approx w_r^*$ near the wall. Hence, in advection-dominated systems, the inherent anisotropy of the mechanical dispersion, i.e., $\alpha_l \gg \alpha_t$ or $r \gg 1$, leads to $D^*_{xx,w} \gg D^*_{zx,r}$, and therefore the interplume spacing increases faster with dispersion than the plume width. This asymmetry results in the fan-flow structure and reduces the transport efficiency.

Below we show how the hydrodynamic dispersion affects the boundary-layer thickness and the convective flux using scaling analysis. In the absence of mechanical dispersion, the balance between advection and diffusion across the near-wall region yields the dimensional boundary-layer thickness

$$\epsilon^* \approx \frac{D_m}{w^*} = \frac{U}{w^*}\frac{D_m}{U} = \frac{1}{w}\frac{H}{\mathrm{Ra}_m} \sim \frac{H}{\mathrm{Ra}_m}, \tag{12}$$

since the dimensionless vertical buoyancy velocity w converges to a constant value at sufficiently large Ra_m [23]. And the dimensional convective flux transported through the upper and lower boundary layers is

$$F^* \approx D_m \frac{\triangle C}{\epsilon^*} \approx w^* \triangle C, \tag{13}$$

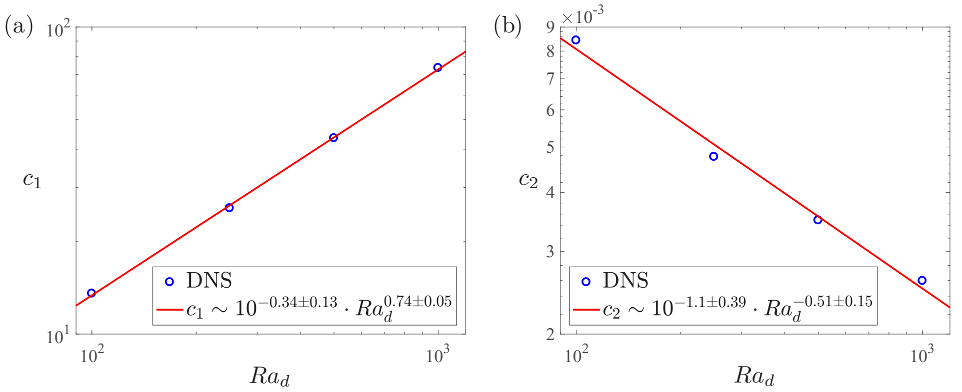

FIG. 7. Variations of the prefactors (a) c_1 and (b) c_2 as a function of Ra_d in the limit of $\mathrm{Ra}_m \to \infty$ at $r = 10$. The solid lines denote the best power-law fit to the DNS data (circles). For each Ra_d, DNS are performed up to $\mathrm{Ra}_m \sim 1000\mathrm{Ra}_d$ to determine c_1 and c_2.

where $\triangle C$ is the concentration difference between the fresh water and the saturated water. As the flux by pure molecular diffusion is $F_m^* \approx D_m \triangle C/H$, the dimensionless convective flux (i.e., the ratio of the transport in the presence of convective motion to the diffusive transport in the absence of fluid motion) can be written as

$$F = \frac{F^*}{F_m^*} \approx \frac{w^* H}{D_m} = \frac{w^*}{U}\frac{UH}{D_m} = w\mathrm{Ra}_m \sim \mathrm{Ra}_m, \tag{14}$$

which has been verified by many numerical studies mentioned in the introduction section.

After adding mechanical dispersion, we can replace the molecular diffusivity D_m with the effective hydrodynamic dispersivity $D_{xz,w}^* \approx D_m + \alpha_t u_w^*$ and rewrite Eq. (12) as

$$\epsilon^* \approx \frac{D_{xz,w}^*}{w^*} \approx \frac{1}{w}\frac{H}{\mathrm{Ra}_m} + \alpha_t = \frac{1}{w}\frac{H}{\mathrm{Ra}_m} + \frac{H}{\mathrm{Ra}_d}. \tag{15}$$

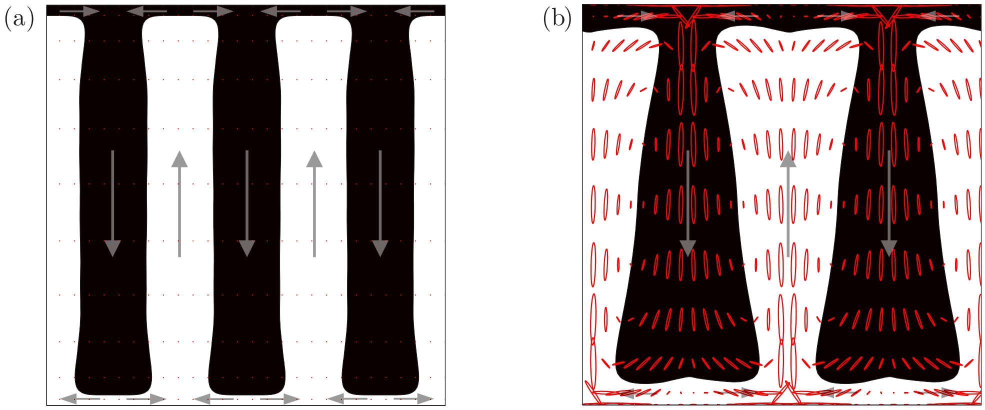

FIG. 8. Schematics showing the distribution of the hydrodynamic dispersion tensor in the form of ellipses. (a) Columnar flow in the absence of mechanical dispersion; (b) fan flow with mechanical dispersion. The arrows denote flow direction. In panel (a), $\mathbf{D}^* = D_m\mathbf{I}$ is homogeneous and isotropic; in panel (b), the anisotropy of the hydrodynamic dispersion leads to an asymmetry between the rising and the descending megaplumes near the walls.

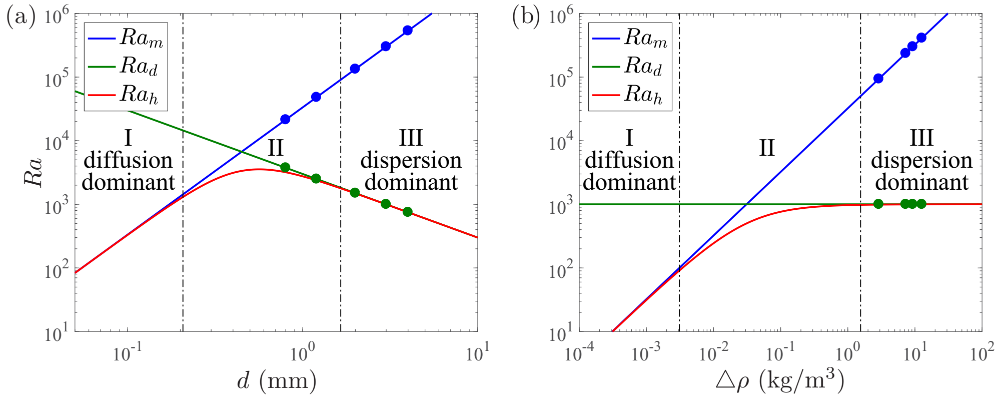

FIG. 9. Variations of control parameters Ra_m and Ra_d as a function of (a) grain size d and (b) density difference $\triangle\rho$ in laboratory experiments. In panel (a), $\triangle\rho = 9.3\,\mathrm{kg/m^3}$; in panel (b), $d = 3$ mm. The dash-dotted lines separate different regimes and the dots denote the experiments in Ref. [36] in terms of Ra_m and Ra_d. In regime I, $\Delta \geqslant 10$, $\mathrm{Ra}_h \sim \mathrm{Ra}_m$, and molecular diffusion dominates the dissipation; in regime II, $0.02 < \Delta < 10$; and in regime III, $\Delta \leqslant 0.02$, $\mathrm{Ra}_h \sim \mathrm{Ra}_d$, and mechanical dispersion dominates the dissipation. In experiments, varying d changes both Ra_m and Ra_d, while varying $\triangle\rho$ only changes Ra_m. Moreover, most of the experiments in Ref. [36] are in the dispersion-dominant regime.

Eq. (12) is recovered as long as the molecular diffusion dominates the dissipation (e.g., $\mathrm{Ra}_d \gg \mathrm{Ra}_m$). Nevertheless, when the dispersion becomes dominant, the dimensionless boundary-layer thickness

$$\epsilon = \frac{\epsilon^*}{H} \approx \frac{1}{\mathrm{Ra}_d}. \tag{16}$$

Therefore, increasing dispersivity thickens the diffusive boundary layer. However, the form of the convective flux in Eq. (13) is not changed, because the reduction of flux due to the increment of boundary-layer thickness is made up by the simultaneous increment of effective diffusion coefficient. Since the buoyancy velocity is only determined by Ra_d as $\mathrm{Ra}_m \to \infty$ [Figs. 2(c) and 4(c)], Eq. (14) becomes

$$F \approx w\mathrm{Ra}_m \sim c(\mathrm{Ra}_d)\mathrm{Ra}_m. \tag{17}$$

Namely, the convective flux is predominantly controlled by Ra_m, but the prefactor is determined by Ra_d.

B. Application for recent laboratory experiments of solutal convection in bead packs

As described in the introduction section, the laboratory experiments on (one-sided) solutal convection in porous media [36] indicate that adjusting Ra_m via changing the density difference $\triangle\rho$ or the grain size d may result in distinct convective characteristics due to hydrodynamic dispersion. In this section, we apply above DNS results and analysis to those experiments. Although our DNS are performed in the two-sided system, they may provide qualitative predictions for the one-sided case due to many common features in convection shared by these two systems [12,17,23,26,27].

In granular media, the mechanical dispersion is proportional to grain size, $\alpha_l \sim d$, so that the appropriate dispersive Rayleigh number is $\mathrm{Ra}_d \approx rH/d$ [38,63]. In experiments [36], increasing d from 0.8 to 4 mm simultaneously increases Ra_m from 1.4×10^4 to 5.0×10^5 ($\triangle\rho = 9.3\,\mathrm{kg/m^3}$) but decreases Ra_d from 3750 to 750 ($H = 30$ cm and assuming $r = 10$), thereby reducing Δ from 0.3 to 1.5×10^{-3} [Fig. 9(a)]. As shown in Fig. 9, most of the experiments in Ref. [36] are in the dispersion-dominant regime, so that the convective pattern is determined by the dispersive Rayleigh

TABLE I. Range of parameters for numerical simulations in Ref. [48].

$\tilde{\mathrm{Ra}}$	$\tilde{S}$	$\tilde{\alpha}$	Ra_m	Ra_d	r	Δ
1000	0.5	0.5	2000	4000	2	2
500	0	0.2	500	∞	5	∞
	0.35		769	7143		9.3
	0.7		1667	3571		2.1
500	0.7	0.1	1667	7143	10	4.3
		0.2		3571	5	2.1
		0.5		1429	2	0.86
		1		714	1	0.43

number, i.e., $C = C(\mathrm{Ra}_d)$, $\delta = \delta(\mathrm{Ra}_d)$, and $\mathbf{u} = \mathbf{u}(\mathrm{Ra}_d)$. Therefore, increasing the grain size d at fixed $\triangle\rho$ intensifies the mechanical dispersion and monotonically coarsens the convective pattern, even if Ra_m increases as well. On the other hand, varying $\triangle\rho$ at fixed d (or k) only changes Ra_m and does not affect the flow pattern set by Ra_d [Fig. 9(b)].

Moreover, for fixed d, the prefactor $c_2(\mathrm{Ra}_d)$ is constant so that the convective flux, $F \sim c_2\mathrm{Ra}_m$, increases linearly with $\triangle\rho$; while for fixed $\triangle\rho$, F is lower than expected at higher d since the flow pattern transitions from columnar flow to fan flow as Ra_d declines [Fig. 2(a)]. However, this reduction in F is accompanied only by a slight reduction in w_m [Fig. 2(c)], which is consistent with the experimental observation that the speed of the fastest fingers increases approximately linearly with both $\triangle\rho$ and k [36,51].

C. Comparison with previous numerical simulations

As mentioned in the introduction section, previous investigations [47,48], utilizing the same Fickian dispersion model, reveal that hydrodynamic dispersion greatly reduces the onset time for convection and enhances the convective mixing. This seems to contradict our numerical simulation results, which indicate that the hydrodynamic dispersion may change the flow pattern and significantly reduce the convective flux (Figs. 1 and 2). Below we show that this discrepancy is mainly due to different nondimensionalizations and their interpretation. It should be noted that in those studies the dispersivity and buoyancy velocity are defined differently by scaling the porosity.

In Ref. [47], the longitudinal dispersivity α_l is introduced to characterize the timescale $\tilde{T} = (D_m + \alpha_l U)/U^2$. For stronger dispersion, i.e., increasing α_l, the timescale $\tilde{T}$ is simultaneously increased, thereby resulting in a smaller dimensionless time $\tilde{t} = t^*/\tilde{T}$ (where t^* is the dimensional time). Thus, as the dispersion is increased, the onset time, evaluated using $\tilde{t}$, can be significantly reduced at fixed molecular Rayleigh number Ra_m and dispersivity ratio r, due to the increase of $\tilde{T}$. How hydrodynamic dispersion affects the onset of convection is beyond the scope of this contribution, but it is necessary to use the same characterize scales for comparison.

In Ref. [48], the molecular diffusivity D_m and the longitudinal dispersivity α_l are combined to define the dimensionless parameters, namely,

$$\tilde{\mathrm{Ra}} = \frac{UH}{D_m + \alpha_l U}, \quad \tilde{S} = \frac{\alpha_l U}{D_m + \alpha_l U}, \quad \tilde{\alpha} = \frac{\alpha_t}{\alpha_l}, \tag{18}$$

where $\tilde{\mathrm{Ra}}$, $\tilde{S}$ and $\tilde{\alpha}$ are, respectively, the effective Rayleigh number, the dispersion strength and the dispersivity ratio. Hence, these parameters are related to our work via

$$\mathrm{Ra}_m = \frac{\tilde{\mathrm{Ra}}}{1 - \tilde{S}}, \quad \mathrm{Ra}_d = \frac{\tilde{\mathrm{Ra}}}{\tilde{\alpha}\tilde{S}}, \quad r = \frac{1}{\tilde{\alpha}}. \tag{19}$$

The range of parameters for numerical simulations in Ref. [48] is shown in Table I. For most of those simulations, the ratio of molecular diffusion to mechanical dispersion $\Delta > 1$, so that the mechanical dispersion is relatively weak. The simulation results in Ref. [48] reveal that with increasing $\tilde{S}$ from 0 to 0.7 at $\tilde{\mathrm{Ra}} = 500$ and $\tilde{\alpha} = 0.2$, the dispersion enhances the mixing and reduces the onset of convection (see in particular their Figs. 5–10).

Although we have shown that the relatively weak mechanical dispersion slightly enhances the convective transport [Fig. 2(a)], in Ref. [48] the increment of flux and the reduction of onset time are because the corresponding molecular Rayleigh number Ra_m, which controls the convective flux, increases simultaneously with $\tilde{S}$ from 500 to 1667 (Table I). Moreover, based on their simulation results at $\tilde{S} = 0.7$ and $\tilde{\mathrm{Ra}} = 500$ for $\tilde{\alpha} = 0.1$, 0.2, 0.5, and 1, it is concluded in Ref. [48] that the dispersivity ratio has a very weak impact on the convective pattern and flux (see in particular their Figs. 11–13), which contradicts our DNS results in Sec. III C.

This discrepancy is actually due to different ranges of parameters: The numerical simulations in Ref. [48] generally focus on the moderate-Ra_m and weak-dispersion regime, while our DNS results indicate that at high Ra_m and for strong mechanical dispersion (e.g., $\mathrm{Ra}_m = 20\,000$ and $\mathrm{Ra}_d = 1000$), the dispersivity ratio significantly affects both the flow pattern and the convective flux.

D. Non-Fickian dispersion

The DNS and analysis presented here are performed in the framework of the classical Fickian dispersion model. This relatively simple model can treat homogeneous porous media under certain conditions and is therefore used in many studies of porous media convection [46–49]. In this case, mechanical dispersion can be described by the standard dispersion tensor, given by (4). This model ignores non-Fickian anomalous behavior, such as the scale dependence and solute tailing, which is commonly observed in solute transport experiments and field observations [40].

However, mathematical formulations that capture such anomalous behavior are typically particle based and hence not amendable to the DNS approach employed in most convection studies. We are not aware of any attempts to model convection in porous media with anomalous dispersion; in fact, to date most numerical studies ignore dispersion entirely. Therefore, even the effect of the Fickian model on the dynamics of convection in porous media is poorly understood.

Hence, this study explores the first-order effect of hydrodynamic dispersion on the convective transport in porous media. Above we have argued that simulations based on the standard model of mechanical dispersion give results that are consistent with experiments performed in homogeneous bead packs [15,36]. It appears that the key characteristics of mechanical dispersion required to explain these experimental data are its velocity and grain size dependence. Anomalous behavior is not evident in these experimental observations, which may be due to the relative homogeneity of the bead packs, the constant geometry of the experiments, and the quasisteady convective dynamics.

V. CONCLUSIONS

We study the effect of dispersion on convective mixing in the 2D Rayleigh-Darcy scenario, where a statistical steady state can be obtained. Our DNS results and analysis reveal that the dynamics of this system in a sufficiently wide domain are controlled by three parameters: The molecular Rayleigh number, Ra_m, the dispersive Rayleigh number, Ra_d, and the dispersivity ratio, r. If mechanical dispersion is the dominant dissipative mechanism, for fixed r the dimensionless convective flux is predominantly controlled by Ra_m, while the convective pattern is determined by Ra_d. This implies that convective flux and pattern are decoupled during porous media convection with dispersion. Moreover, when mechanical dispersion dominates the hydrodynamic dispersion, for fixed $(\mathrm{Ra}_m, \mathrm{Ra}_d)$ both the flow pattern and the flux are significantly affected by r: The high-Ra_m convection remains a columnar structure at $r = 1$ but transitions to a fan-flow structure at $r \gg 1$, which reduces the convective flux.

Here we confirm that the linear flux scaling, $F \sim \mathrm{Ra}_m$, also holds in the presence of hydrodynamic dispersion. However, this is only true if Ra_d remains constant (e.g., same media property), since Ra_d determines the prefactor of the scaling law. In practice, Ra_m and Ra_d commonly change together, because changes in grain size affect both permeability and dispersivity. This makes it difficult to observe the linear flux scaling in bead packs, where the flux does not increase linearly with permeability.

More specifically, our simulations in advection-dominated systems ($r = 10$) show the following:

(1) For $\Delta = \mathrm{Ra}_d/\mathrm{Ra}_m > O(1)$, molecular diffusion dominates the hydrodynamic dispersion, although relatively weak mechanical dispersion slightly enhances the convective transport.

(2) For $0.02 \lesssim \Delta < O(1)$, both the molecular diffusion and the mechanical dispersion significantly affect the convective pattern and flux.

(3) For $\Delta < 0.02$, mechanical dispersion dominates the hydrodynamic dispersion: The flow pattern is determined by Ra_d, e.g., $C = C(\mathrm{Ra}_d)$, $\delta = \delta(\mathrm{Ra}_d)$, and $\mathbf{u} = \mathbf{u}(\mathrm{Ra}_d)$, while the flux is predominantly controlled by Ra_m, e.g., $F \sim c(\mathrm{Ra}_d)\mathrm{Ra}_m$.

(4) In the limit of $\mathrm{Ra}_m \to \infty$, the flow still exhibits the columnar structure for $\mathrm{Ra}_d > 5000$; however, for $\mathrm{Ra}_d < 5000$ the convection transitions to the fan-flow structure, due to the inherent anisotropy of mechanical dispersion, which reduces the convective flux.

We note that the above criterions may vary quantitatively in other (e.g., the one-sided) convective systems, and many characteristics shown here are unlikely to be observed in the Hele-Shaw experiments, due to the absence of transverse mechanical dispersion [64].

ACKNOWLEDGMENTS

This work was supported as part of the Center for Frontiers in Subsurface Energy Security, an Energy Frontier Research Center funded by the US Department of Energy, Office of Science, Basic Energy Sciences, under Award No. DE-SC0001114. B.W. acknowledges the Peter O'Donnell, Jr. Postdoctoral Fellowship through the Institute of Computational and Engineering and Science at the University of Texas at Austin.

[1] C. W. Horton and F. T. Rogers, Convection currents in a porous medium, J. Appl. Phys. **16**, 367 (1945).

[2] E. R. Lapwood, Convection of a fluid in a porous medium, Proc. Cambridge Philos. Soc. **44**, 508 (1948).

[3] O. M. Phillips, *Geological Fluid Dynamics: Sub-surface Flow and Reactions* (Cambridge University Press, Cambridge, UK, 2009).

[4] D. A. Nield and A. Bejan, *Convection in Porous Media*, 3rd ed. (Springer, New York, 2006).

[5] F. M. Orr, Onshore geologic storage of CO_2, Science **325**, 1656 (2009).

[6] K. Michael, A. Golab, V. Shulakova, J. Ennis-King, G. Allinson, S. Sharma, and T. Aiken, Geological storage of CO_2 in saline aquifers: A review of the experience from existing storage operations, Int. J. Greenhouse Gas Control **4**, 659 (2010).

[7] M. L. Szulczewski, C. W. MacMinn, H. J. Herzog, and R. Juanes, Lifetime of carbon capture and storage as a climate-change mitigation technology, PNAS **109**, 5185 (2012).

[8] G. J. Weir, S. P. White, and W. M. Kissling, Reservoir storage and containment of greenhouse gases, II: Vapour-entry pressures, Transp. Porous Media **23**, 61 (1996).

[9] J. P. Ennis-King and L. Paterson, Role of convective mixing in the long-term storage of carbon dioxide in deep saline formations, SPE J. **10**, 349 (2005).

[10] K. J. Sathaye, M. A. Hesse, M. Cassidy, and D. F. Stockli, Constraints on the magnitude and rate of CO_2 dissolution at Bravo Dome natural gas field, PNAS **111**, 15332 (2014).

[11] D. Akhbari and M. A. Hesse, Causes of underpressure in natural CO_2 reservoirs and implications for geological storage, Geology **45**, 47 (2017).

[12] B. Wen, D. Akhbari, L. Zhang, and M. A. Hesse, Convective carbon dioxide dissolution in a closed porous medium at low pressure, J. Fluid Mech. **854**, 56 (2018).

[13] J. J. Roberts, R. A. Wood, and R. S. Haszeldine, Assessing the health risks of natural CO_2 seeps in Italy, PNAS **108**, 16545 (2011).

[14] A. Riaz, M. Hesse, H. A. Tchelepi, and F. M. Orr, Onset of convection in a gravitationally unstable diffusive boundary layer in porous media, J. Fluid Mech. **548**, 87 (2006).

[15] J. A. Neufeld, M. A. Hesse, A. Riaz, M. A. Hallworth, H. A. Tchelepi, and H. E. Huppert, Convective dissolution of carbon dioxide in saline aquifers, Geophys. Res. Lett. **37**, L22404 (2010).

[16] S. Backhaus, K. Turitsyn, and R. E. Ecke, Convective Instability and Mass Transport of Diffusion Layers in a Hele-Shaw Geometry, Phys. Rev. Lett. **106**, 104501 (2011).

[17] D. R. Hewitt, J. A. Neufeld, and J. R. Lister, Stability of columnar convection in a porous medium, J. Fluid Mech. **737**, 205 (2013).

[18] M. L. Szulczewski, M. A. Hesse, and R. Juanes, Carbon dioxide dissolution in structural and stratigraphic traps, J. Fluid Mech. **736**, 287 (2013).

[19] A. C. Slim, Solutal-convection regimes in a two-dimensional porous medium, J. Fluid Mech. **741**, 461 (2014).

[20] Z. Shi, B. Wen, M. A. Hesse, T. T. Tsotsis, and K. Jessen, Measurement and modeling of CO_2 mass transfer in brine at reservoir conditions, Adv. Water Resour. **113**, 100 (2018).

[21] M. D. Graham and P. H. Steen, Strongly interacting traveling waves and quasiperiodic dynamics in porous medium convection, Phys. D (Amsterdam, Neth.) **54**, 331 (1992).

[22] J. Otero, L. A. Dontcheva, H. Johnston, R. A. Worthing, A. Kurganov, G. Petrova, and C. R. Doering, High-Rayleigh-number convection in a fluid-saturated porous layer, J. Fluid Mech. **500**, 263 (2004).

[23] D. R. Hewitt, J. A. Neufeld, and J. R. Lister, Ultimate Regime of High Rayleigh Number Convection in a Porous Medium, Phys. Rev. Lett. **108**, 224503 (2012).

[24] D. R. Hewitt, J. A. Neufeld, and J. R. Lister, High Rayleigh number convection in a three-dimensional porous medium, J. Fluid Mech. **748**, 879 (2014).

[25] B. Wen, L. T. Corson, and G. P. Chini, Structure and stability of steady porous medium convection at large Rayleigh number, J. Fluid Mech. **772**, 197 (2015).

[26] M. D. Paoli, F. Zonta, and A. Soldati, Influence of anisotropic permeability on convection in porous media: Implications for geological CO_2 sequestration, Phys. Fluids **28**, 056601 (2016).

[27] M. D. Paoli, F. Zonta, and A. Soldati, Dissolution in anisotropic porous media: Modelling convection regimes from onset to shutdown, Phys. Fluids **29**, 026601 (2017).

[28] D. R. Hewitt and J. R. Lister, Stability of three-dimensional columnar convection in a porous medium, J. Fluid Mech. **829**, 89 (2017).

[29] B. Wen and G. P. Chini, Inclined porous medium convection at large Rayleigh number, J. Fluid Mech. **837**, 670 (2018).

[30] G. S. H. Pau, J. B. Bell, K. Pruess, A. S. Almgren, M. J. Lijewski, and K. Zhang, High-resolution simulation and characterization of density-driven flow in CO_2 storage in saline aquifers, Adv. Water Resour. **33**, 443 (2010).

[31] J. J. Hidalgo, J. Fe, L. Cueto-Felgueroso, and R. Juanes, Scaling of Convective Mixing in Porous Media, Phys. Rev. Lett. **109**, 264503 (2012).

[32] B. Wen, N. Dianati, E. Lunasin, G. P. Chini, and C. R. Doering, New upper bounds and reduced dynamical modeling for Rayleigh-Bénard convection in a fluid saturated porous layer, Commun. Nonlinear Sci. Numer. Simul. **17**, 2191 (2012).

[33] B. Wen, G. P. Chini, N. Dianati, and C. R. Doering, Computational approaches to aspect-ratio-dependent upper bounds and heat flux in porous medium convection, Phys. Lett. A **377**, 2931 (2013).

[34] P. Hassanzadeh, G. P. Chini, and C. R. Doering, Wall to wall optimal transport, J. Fluid Mech. **751**, 627 (2014).

[35] M. A. Hesse, Mathematical modeling and multiscale simulation of carbon dioxide storage in saline aquifers, Ph.D. thesis, Stanford University, Stanford, CA, 2008.

[36] Y. Liang, B. Wen, M. Hesse, and D. DiCarlo, Effect of dispersion on solutal convection in porous media, Geophys. Res. Lett. **45**, 9690 (2018).

[37] G. De Josselin De Jong, Longitudinal and transverse diffusion in granular deposits, Eos, Trans. Am. Geophys. Union **39**, 67 (1958).

[38] P. G. Saffman, A theory of dispersion in a porous medium, J. Fluid Mech. **6**, 321 (1959).

[39] Y. Bachmat and J. Bear, The general equations of hydrodynamic dispersion in homogeneous, isotropic, porous media, J. Geophys. Res. **69**, 2561 (1964).

[40] B. Berkowitz, A. Cortis, M. Dentz, and H. Scher, Modeling non-Fickian transport in geological formations as a continuous time random walk, Rev. Geophys. **44**, RG2003 (2006).

[41] L. F. Konikow, The secret to successful solute-transport modeling, Groundwater **49**, 144 (2011).

[42] M. Dentz, M. Icardi, and J. J. Hidalgo, Mechanisms of dispersion in a porous medium, J. Fluid Mech. **841**, 851 (2018).

[43] J. Bear, On the tensor form of dispersion in porous media, J. Geophys. Res. **66**, 1185 (1961).

[44] A. E. Scheidegger, General theory of dispersion in porous media, J. Geophys. Res. **66**, 3273 (1961).

[45] G. de Josselin de Jong and M. J. Bossen, Discussion of paper by Jacob Bear, "On the tensor form of dispersion in porous media", J. Geophys. Res. **66**, 3623 (1961).

[46] K. Ghesmat and J. Azaiez, Viscous fingering instability in porous media: Effect of anisotropic velocity-dependent dispersion tensor, Transp. Porous Media **73**, 297 (2008).

[47] J. J. Hidalgo and J. Carrera, Effect of dispersion on the onset of convection during CO_2 sequestration, J. Fluid Mech. **640**, 441 (2009).

[48] K. Ghesmat, H. Hassanzadeh, and J. Abedi, The effect of anisotropic dispersion on the convective mixing in long-term CO_2 storage in saline aquifers, AIChE J. **57**, 561 (2011).

[49] H. Emami-Meybodi, H. Hassanzadeh, and J. Ennis-King, CO_2 dissolution in the presence of background flow of deep saline aquifers, Water Resour. Res. **51**, 2595 (2015).

[50] H. Emami-Meybodi, Stability analysis of dissolution-driven convection in porous media, Phys. Fluids **29**, 014102 (2017).

[51] L. Wang, Y. Nakanishi, A. Hyodo, and T. Suekane, Three-dimensional structure of natural convection in a porous medium: Effect of dispersion on finger structure, Int. J. Greenh. Gas Control **53**, 274 (2016).

[52] Y. Nakanishi, A. Hyodo, L. Wang, and T. Suekane, Experimental study of 3D Rayleigh-Taylor convection between miscible fluids in a porous medium, Adv. Water Resour. **97**, 224 (2016).

[53] T. Suekane, J. Ono, A. Hyodo, and Y. Nagatsu, Three-dimensional viscous fingering of miscible fluids in porous media, Phys. Rev. Fluids **2**, 103902 (2017).

[54] Y. Liang, Scaling of solutal convection in porous media, Ph.D. thesis, The University of Texas at Austin, Austin, TX, 2017.

[55] E. Abarca, J. Carrera, X. Sánchez-Vila, and M. Dentz, Anisotropic dispersive Henry problem, Adv. Water Resour. **30**, 913 (2007).

[56] N. Nikitin, Third-order-accurate semi-implicit Runge-Kutta scheme for incompressible Navier-Stokes equations, Int. J. Numer. Meth. Fluids **51**, 221 (2006).

[57] L. W. Gelhar, C. Welty, and K. R. Rehfeldt, A critical review of data on field-scale dispersion in aquifers, Water Resour. Res. **28**, 1955 (1992).

[58] T. K. Perkins and O. C. Johnston, A review of diffusion and dispersion in porous media, Soc. Pet. Eng. J. **3**, 70 (1963).

[59] J. D. Seymour and P. T. Callaghan, Generalized approach to NMR analysis of flow and dispersion in porous media, AIChE J. **43**, 2096 (1997).

[60] A. A. Khrapitchev and P. T. Callaghan, Reversible and irreversible dispersion in a porous medium, Phys. Fluids **15**, 2649 (2003).

[61] B. Bijeljic and M. J. Blunt, Porescale modeling of transverse dispersion in porous media, Water Resour. Res. **43**, W12S11 (2007).

[62] M. Muniruzzaman and M. Rolle, Experimental investigation of the impact of compound-specific dispersion and electrostatic interactions on transient transport and solute breakthrough, Water Resour. Res. **53**, 1189 (2017).

[63] S. E. Oswald and W. Kinzelbach, Three-dimensional physical benchmark experiments to test variable-density flow models, J. Hydrol. **290**, 22 (2004).

[64] R. Maes, G. Rousseaux, B. Scheid, M. Mishra, P. Colinet, and A. De Wit, Experimental study of dispersion and miscible viscous fingering of initially circular samples in Hele-Shaw cells, Phys. Fluids **22**, 123104 (2010).